

Imprints of light dark matter on the evolution of cosmic neutrinos

Isaac R. Wang^{a,b} and Xun-Jie Xu^c

^a*Theory Division, Fermi National Accelerator Laboratory, Batavia, IL 60510, USA*

^b*New High Energy Theory Center, Department of Physics and Astronomy, Rutgers University, Piscataway, NJ 08854, USA*

^c*Institute of High Energy Physics, Chinese Academy of Sciences, Beijing 100049, China*

E-mail: isaacw@fnal.gov, xuxj@ihep.ac.cn

ABSTRACT: Neutrinos are often considered as a portal to new physics beyond the Standard Model (SM) and might possess phenomenologically interesting interactions with dark matter (DM). This paper examines the cosmological imprints of DM that interacts with and is produced from SM neutrinos at temperatures below the MeV scale. We take a model-independent approach to compute the evolution of DM in this framework and present analytic results which agree well with numerical ones. Both freeze-in and freeze-out regimes are included in our analysis. Furthermore, we demonstrate that the thermal evolution of neutrinos might be substantially affected by their interaction with DM. We highlight two distinctive imprints of such DM on neutrinos: (i) a large, negative contribution to N_{eff} , which is close to the current experimental limits and will readily be probed by future experiments; (ii) spectral distortion of the cosmic neutrino background ($C\nu B$) due to DM annihilating into neutrinos, a potentially important effect for the ongoing experimental efforts to detect $C\nu B$.

Contents

1	Introduction	1
2	Evolution of the dark sector	2
2.1	A schematic of the framework	2
2.2	The Boltzmann equation	4
2.3	Analytic solution in the high- T regime	6
2.4	Analytic solution in the low- T regime	6
2.5	DM relic abundance	8
2.6	Model-specific analyses	9
3	Cosmological consequences and constraints	10
3.1	N_{eff} constraints	10
3.2	Lyman- α constraint	11
3.3	Distortion of $C\nu B$	13
4	Summary and conclusions	16
A	Collision terms and thermally-averaged cross sections	17
B	Useful approximations in the freeze-out regime	19
C	Solving Boltzmann equations for three coupled species	20

1 Introduction

Dark matter (DM) has been an enduring mystery for decades. As extensive cosmological and astrophysical evidence supports its existence, DM poses one of the major challenges to the success of the Standard Model (SM) of particle physics. To date, DM searches in direct or indirect detection experiments, which rely on the couplings of DM with nucleons or electromagnetically-interacting particles, have not yet yielded any conclusive signals of DM. Therefore, it is plausible to consider that DM may reside in a hidden dark sector that barely interacts with quarks or charged leptons. For instance, the dark sector could be connected to the SM only via the neutrino portal [1–11], suggesting a scenario where DM predominantly interacts with neutrinos rather than other SM particles. This scenario, despite being generically difficult to probe in direct or indirect detection experiments, may still leave discernible cosmological imprints.

Indeed, as already investigated in numerous studies, the presence of DM-neutrino interactions may cause cosmologically observable effects. These include modifying the cosmic

microwave background (CMB) anisotropies [12–15], altering the big bang nucleosynthesis (BBN) predictions [16, 17], reducing small-scale structures [18, 19], etc.

In this work, we focus on the epoch when the SM neutrinos (ν) have decoupled from the thermal bath. We examine a generic framework where a light DM candidate, denoted by χ , interacts predominantly with ν . The interaction leads to the conversion $\nu\bar{\nu} \leftrightarrow \chi\bar{\chi}$ and is responsible for the DM abundance, via either the freeze-in [20] or the freeze-out [21] mechanism.

Due to the conversion between χ and ν , the effective number of neutrino species, N_{eff} , could receive a potentially large correction, which can be positive [22, 23] or negative [8], depending on the strength and energy scale of the interaction. While a positive correction to N_{eff} is rather common in various new physics scenarios (see e.g. Ref. [24–30]), a negative one is relatively rare. In Ref. [8], the negative correction is obtained only in the freeze-in regime but in fact this can also occur in the freeze-out regime, as we will show in this work.

The impact of such DM is not limited to N_{eff} ; it also extends to the energy distribution of cosmic neutrinos. The process $\chi\bar{\chi} \rightarrow \nu\bar{\nu}$ continues to generate neutrinos until today at a low, yet non-vanishing rate after its decoupling. This would distort the high-energy tail of the cosmic neutrino background (C ν B) from the exponentially suppressed form to a power-law form, and hence substantially enhance the neutrino flux of C ν B at high energies. In particular, we will show that the enhanced C ν B tail yields a neutrino flux much higher than that from BBN isotope decays and solar thermal production in the sub-eV to keV range.

This paper is organized as follows. In Sec. 2, we calculate the thermal evolution of DM and neutrinos in the presence of DM-neutrino interactions. In Sec. 3, we evaluate the impact of DM on N_{eff} and C ν B distortion, as well as the Lyman- α constraints on light DM. Finally we conclude in Sec. 4 and relegate some details to appendices.

2 Evolution of the dark sector

2.1 A schematic of the framework

Figure 1 illustrates schematically the evolution of DM abundance in our framework. In the early universe when the temperature T is well above all mass scales involved in $\nu\bar{\nu} \leftrightarrow \chi\bar{\chi}$, the reaction rate $\Gamma \propto T$ can be inefficient in comparison to the Hubble expansion rate $H \propto T^2$. Within this epoch, χ is not in equilibrium with ν , and the number of χ particles in a comoving volume keeps increasing due to $\nu\bar{\nu} \rightarrow \chi\bar{\chi}$ towards its equilibrium value. We refer to this epoch as the production phase of DM.

Depending on the strength of the interaction, the subsequent evolution may or may not be able to drive χ into equilibrium, as demonstrated by the blue and green curves in Fig. 1, respectively. In the former case, the DM number density, n_χ , is kept at its equilibrium value until n_χ is too low to maintain thermal equilibrium, leading to the well-known freeze-out mechanism. While for the latter case, χ is produced at a low reaction rate which is always below the Hubble expansion rate, corresponding to the freeze-in mechanism.

After χ has decoupled with ν , the process $\chi\bar{\chi} \rightarrow \nu\bar{\nu}$ may lead to C ν B distortion. Note that there is a difference between chemical decoupling and kinetic decoupling. The chemical

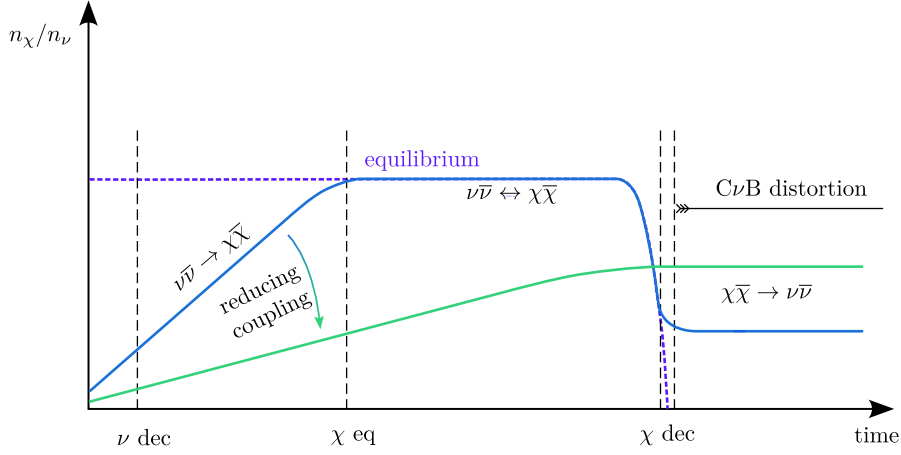


Figure 1. A schematic showing the evolution of the DM abundance in our framework. Here “ ν dec”, “ χ eq”, and “ χ dec” indicate the moments of neutrino decoupling, χ reaching equilibrium, and χ decoupling. The period between “ χ eq”, and “ χ dec” may be absent for scenarios with sufficiently weak interactions, such as the green curve. For “ χ dec”, we plot two vertical dashed lines to represent the difference between chemical and kinetic decoupling. C ν B distortion due to $\chi\bar{\chi} \rightarrow \nu\bar{\nu}$ only starts from the kinetic decoupling.

equilibrium is maintained by $\nu\bar{\nu} \leftrightarrow \chi\bar{\chi}$ which can alter particle numbers of ν or χ , while the kinetic equilibrium is maintained by processes that can transfer the kinetic energy of ν and χ from one to the other. Hence the kinetic equilibrium can be maintained by not only $\nu\bar{\nu} \leftrightarrow \chi\bar{\chi}$ but also the particle-number-conserving process $\nu\chi \leftrightarrow \nu\chi$. Consequently, kinetic equilibrium typically lasts longer than chemical equilibrium, as we will see in a specific example in Sec. 3.3. As long as the kinetic equilibrium is maintained, it is justified to assume

$$f_\nu(p) \propto f_\nu^{\text{eq}}(p), \quad f_\chi(p) \propto f_\chi^{\text{eq}}(p), \quad (2.1)$$

where $f_{\nu/\chi}$ denotes the phase space distribution function of ν/χ , and $f_{\nu,\chi}^{\text{eq}}$ denotes the equilibrium value of $f_{\nu/\chi}$ when both kinetic equilibrium and chemical equilibrium are reached. After kinetic decoupling, however, f_ν and f_χ are unable to maintain the shape in Eq. (2.1). In particular, due to DM annihilation, $\chi\bar{\chi} \rightarrow \nu\bar{\nu}$, which keeps generating neutrinos until today at a very low yet non-vanishing rate, we expect that today’s f_ν should be distorted. This is indicated in Fig. 1 as C ν B distortion.

In what follows, we will study quantitatively the evolution depicted in Fig. 1, and scrutinize these effects on cosmic neutrinos.

Before we start, we shall clarify our notation of temperature in this work. Since neutrinos and photons have different temperatures after e^+e^- annihilation, we denote them by T_ν and T_γ when they need to be distinguished. Otherwise, we use T to denote a generic temperature. More strictly, we define T as

$$T \equiv T_\star \frac{a_\star}{a}, \quad (2.2)$$

where T_\star denotes a pivot temperature that can be set at any point before neutrino decoupling (e.g. $T_\star = 10$ MeV), and a is the scale factor with “ \star ” indicating the pivot value.

2.2 The Boltzmann equation

We start with a model-independent analysis by considering the thermally averaged cross section, $\langle\sigma v\rangle$, which has been extensively used in DM studies, in particular, in non-relativistic freeze-out scenarios. We should mention here that $\langle\sigma v\rangle$ can be rigorously defined also in the relativistic regime [31], making it applicable to both freeze-in and freeze-out scenarios. Moreover, we will show that it can be parametrized by two simple parameters which suffice for an accurate description of the collision terms in specific models (see Fig. 2). Complete analyses for specific models are also conducted in this work, arriving at similar results (see Sec. 2.6 and Fig. 4).

Given the thermally averaged cross section for $\nu\bar{\nu} \leftrightarrow \chi\bar{\chi}$, the number density of DM is governed by the following Boltzmann equation:

$$\frac{dn_\chi}{dt} + 3Hn_\chi = -N_\nu\langle\sigma v\rangle(n_\chi^2 - n_\nu^2 B^2), \quad (2.3)$$

where n_χ and n_ν denote the number densities of χ and ν , H is the Hubble parameter, $N_\nu = 3$ accounts for the three neutrino flavors, and the Boltzmann suppression factor B is defined as

$$B \equiv \frac{x^2}{2} K_2(x), \quad x \equiv \frac{m_\chi}{T}, \quad (2.4)$$

where m_χ is the mass of χ . Eq. (2.3) together with the B factor in Eq. (2.4) can be obtained by reformulating the conventional collision terms into the $\langle\sigma v\rangle$ form, assuming the validity of Eq. (2.1) and Boltzmann statistics. In Appendix A, we briefly review the derivation of Eq. (2.3).

Note that in our convention, n_ν is defined as the neutrino number density of a single flavor, without including antineutrinos. The same convention also applies to n_χ . In this work, we assume that DM-neutrino interactions are flavor-universal and flavor-diagonal.

When ν is converted to χ via $\nu\bar{\nu} \leftrightarrow \chi\bar{\chi}$, the total number of ν and χ in a comoving volume is conserved if they do not interact with other particles. Hence, we define

$$n_{\chi\nu} \equiv n_\chi + N_\nu n_\nu, \quad \bar{n}_{\chi\nu} \equiv \bar{n}_\chi + N_\nu \bar{n}_\nu, \quad (2.5)$$

where $\bar{n}_\chi \equiv n_\chi a^3$ and $\bar{n}_\nu \equiv n_\nu a^3$, with a the scale factor. After neutrino decoupling, $\bar{n}_{\chi\nu}$ should be a constant, $d\bar{n}_{\chi\nu}/dt = 0$.

The thermally averaged cross section $\langle\sigma v\rangle$ is defined as

$$\langle\sigma v\rangle \equiv n_\chi^{-2} \int f_\chi(p_1) f_\chi(p_2) |\mathcal{M}|^2 (2\pi\delta)^4 d\Pi_1 d\Pi_2 d\Pi_3 d\Pi_4, \quad (2.6)$$

where $d\Pi_i \equiv \frac{d^3 p_i}{(2\pi)^3 2E_i}$ with i indicating the i -th particle in $\chi\bar{\chi} \rightarrow \nu\bar{\nu}$, $|\mathcal{M}|^2$ denotes the squared amplitude of the reaction, and $(2\pi\delta)^4 \equiv (2\pi)^4 \delta^4(p_1 + p_2 - p_3 - p_4)$. Despite its common use in non-relativistic freeze-out, $\langle\sigma v\rangle$ is well defined in the relativistic regime as well. So Eq. (2.6) can be readily applied to both non-relativistic and relativistic annihilation.

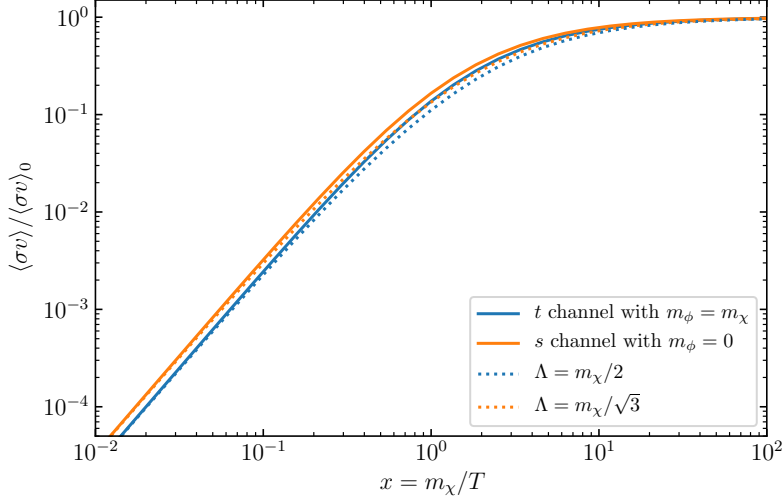


Figure 2. The temperature dependence of $\langle\sigma v\rangle$. The two solid curves represent two possible UV completions of the process $2\nu \leftrightarrow 2\chi$ through an s - or t -channel mediator ϕ —see Eqs. (2.9) and (2.10). The dotted curves represent our phenomenological modeling of $\langle\sigma v\rangle$ given in Eq. (2.8), with the free parameter Λ determined by the high- T limits of the solid curves.

Let us investigate the behavior of $\langle\sigma v\rangle$ at different temperatures. In the low- T limit when χ becomes non-relativistic, $\langle\sigma v\rangle$ can be regarded as a constant, $\langle\sigma v\rangle = \langle\sigma v\rangle_0$, provided that $\chi\bar{\chi} \rightarrow \nu\bar{\nu}$ is s -wave annihilation. In the high- T limit when all masses are well below T and hence negligible, we expect from a simple dimensional analysis that

$$\langle\sigma v\rangle \propto T^{-2}. \quad (2.7)$$

Therefore, for practical use, we parametrize $\langle\sigma v\rangle$ as

$$\langle\sigma v\rangle \approx \frac{\langle\sigma v\rangle_0}{(1 + T/\Lambda)^2}, \quad (2.8)$$

where Λ represents the energy scale (typically the highest mass of those involved in the annihilation processes) when $\langle\sigma v\rangle$ starts to transition from its constant value $\langle\sigma v\rangle_0$ to the T^{-2} form.

Eq. (2.8) provides a simple parametrization of $\langle\sigma v\rangle$ with only two free parameters, $\langle\sigma v\rangle_0$ and Λ . Despite its simplicity, Eq. (2.8) can accurately account for the temperature dependence of $\langle\sigma v\rangle$ in a specific model.

For illustration, let us consider two models where $\nu\bar{\nu} \leftrightarrow \chi\bar{\chi}$ is mediated by either an s -channel vector mediator ϕ^μ or a t -channel scalar mediator ϕ :

$$s\text{-channel model: } \mathcal{L} \supset g_\nu \nu^\dagger \bar{\sigma}^\mu \phi_\mu \nu + g_\chi \chi^\dagger \bar{\sigma}^\mu \phi_\mu \chi, \quad (2.9)$$

$$t\text{-channel model: } \mathcal{L} \supset y_\chi \nu \chi \phi, \quad (2.10)$$

where $g_{\nu/\chi}$ and y_χ are dimensionless couplings. We denote the mediator mass by m_ϕ . It should be above m_χ in the t -channel model as required by the stability of χ , while in the s -channel model, it can be arbitrarily light.

For the above specific models, the thermally-averaged cross sections are computed in Appendix A. The numerical results of $\langle\sigma v\rangle$ for the two models are presented in Fig. 2 by the solid curves. In certain limits, they have analytic forms:

$$\langle\sigma v\rangle^{(t)} \approx \frac{y_\chi^4}{32\pi m_\chi^2} \times \begin{cases} 1 & \text{for } x \gg 1 \\ \frac{1}{4}x^2 & \text{for } x \ll 1 \end{cases}, \quad \langle\sigma v\rangle^{(s)} \approx \frac{g_\nu^2 g_\chi^2}{32\pi m_\chi^2} \times \begin{cases} 1 & \text{for } x \gg 1 \\ \frac{1}{3}x^2 & \text{for } x \ll 1 \end{cases}, \quad (2.11)$$

where the superscripts (t) and (s) indicate the type of the mediator. By fitting Eq. (2.8) to Eq. (2.11), we obtain $\Lambda = m_\chi/2$ and $\Lambda = m_\chi/\sqrt{3}$ for $\langle\sigma v\rangle^{(t)}$ and $\langle\sigma v\rangle^{(s)}$, respectively. As is shown in Fig. 2, the dotted curves produced from Eq. (2.8) fit the solid curves rather accurately.

2.3 Analytic solution in the high- T regime

In the high- T regime, Eq. (2.8) gives $\langle\sigma v\rangle \approx \langle\sigma v\rangle_0 \Lambda^2/T^2$. In addition, the Boltzmann suppression factor B in Eq. (2.3) can be neglected, $B \approx 1$. In this regime, the Boltzmann equation can be solved analytically, as can be seen by rewriting Eq. (2.3) as follows:

$$\frac{d\bar{n}_\chi}{da} = N_\nu \frac{\langle\sigma v\rangle_0}{H_\Lambda a_\Lambda^4} (\bar{n}_\nu^2 - \bar{n}_\chi^2), \quad (2.12)$$

where a_Λ and H_Λ denote the values of a and H at $T = \Lambda$. Using the conservation of $\bar{n}_{\chi\nu}$ introduced in Eq. (2.5) and substituting $\bar{n}_\nu = (\bar{n}_{\chi\nu} - \bar{n}_\chi)/N_\nu$ into Eq. (2.12), we obtain the following analytic solution:

$$\bar{n}_\chi = \bar{n}_{\chi\nu} \frac{\mathcal{E} - 1}{4\mathcal{E} + 2}, \quad (2.13)$$

with

$$\mathcal{E} = \exp\left(2R_\Lambda \frac{a}{a_\Lambda}\right), \quad R_\Lambda \equiv \frac{\langle\sigma v\rangle_0 \bar{n}_{\chi\nu}}{H_\Lambda a_\Lambda^3} = \frac{\langle\sigma v\rangle_0 n_{\chi\nu}}{H} \Big|_{T \rightarrow \Lambda}. \quad (2.14)$$

Here we have already taken $N_\nu = 3$. For a more general value of N_ν , $4\mathcal{E} + 2$ in Eq. (2.13) should be replaced by $(N_\nu + 1)\mathcal{E} + N_\nu - 1$.

The dimensionless ratio R_Λ in Eq. (2.14) quantifies the rapidity of \bar{n}_χ approaching its equilibrium value. For $R_\Lambda \gg 1$, we expect that $\mathcal{E} \gg 1$ at $a \gtrsim a_\Lambda/R_\Lambda$. Consequently, Eq. (2.13) gives $\bar{n}_\chi = \bar{n}_{\chi\nu}/4$, implying that χ reaches the same number density as ν (per flavor). For $R_\Lambda \ll 1$, χ cannot reach equilibrium before $a = a_\Lambda$ while the subsequent evolution would further reduce $\langle\sigma v\rangle n_{\chi\nu}/H$ because at $T \ll \Lambda$ we have $\langle\sigma v\rangle n_{\chi\nu} \propto a^{-3}$ and $H \propto a^{-2}$. Therefore, $R_\Lambda \gtrsim 1$ can be used as the criteria to infer whether χ is able to reach equilibrium.

In the left panel of Fig. 3, we plot Eq. (2.13) by the red dashed curve for $m_\chi = 10$ keV, $\Lambda = m_\chi/\sqrt{3}$, and $\langle\sigma v\rangle_0 = 1.6 \times 10^{-21} m_\chi^2$, corresponding to $R_\Lambda = 56.8$. The curve agrees well with the numerical solution in the high- T regime.

2.4 Analytic solution in the low- T regime

In the low- T regime when $T \ll \Lambda$, Eq. (2.8) gives $\langle\sigma v\rangle \approx \langle\sigma v\rangle_0$. By defining the following variables

$$y = \frac{N_\nu \langle\sigma v\rangle_0}{H_m a_m^3} \bar{n}_\chi, \quad y_0 = \frac{N_\nu \langle\sigma v\rangle_0}{H_m a_m^3} \bar{n}_\nu B, \quad x \equiv \frac{m_\chi}{T}, \quad (2.15)$$

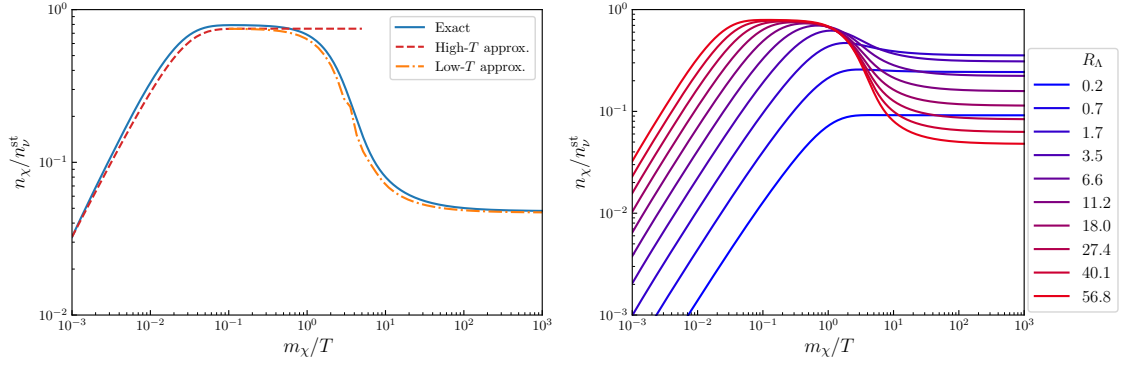


Figure 3. Left panel: analytic solutions obtained in the high- T (dashed curve) and low- T (dash-dotted) approximations compared with the numerical one (blue). Right panel: numerical solutions for R_Λ varying from the weakly-coupled regime ($R_\Lambda \ll 1$) to the strongly-coupled regime ($R_\Lambda \gg 1$). The y -axes have been normalized by n_ν^{st} which is the value of n_ν in the standard cosmological model.

where a_m and H_m denote the values of a and H at $T = m_\chi$, we can rewrite Eq. (2.3) into the form of a Riccati equation:

$$y'(x) = -\frac{y(x)^2 - y_0(x)^2}{x^2}. \quad (2.16)$$

In general, Eq. (2.16) cannot be solved analytically. But when y_0 is negligibly small (it is Boltzmann suppressed at $x \gg 1$), Eq. (2.16) can be solved analytically in the limit of vanishing y_0 . Following the computation in Appendix B, we find that the following piecewise function can approximate the exact solution quite accurately:

$$y = \begin{cases} \frac{x}{x/x_{\text{f.o}} - 1} & x > 2x_{\text{f.o}} \\ y_0(x) & x < x_{\text{f.o}} \\ \frac{x y_{\text{f.o}}}{x(\xi - 1) + x_{\text{f.o}}(2 - \xi)} & x \in [x_{\text{f.o}}, 2x_{\text{f.o}}] \end{cases}, \quad (2.17)$$

where $y_{\text{f.o}} \equiv y_0(x_{\text{f.o}})$ and $\xi \equiv y_{\text{f.o}}/x_{\text{f.o}}$ with $x_{\text{f.o}}$ the freeze-out value of x . In Appendix B, we find that $x_{\text{f.o}}$ can be approximately evaluated by

$$x_{\text{f.o}} \simeq 0.048 + 1.73 \log_{10}(y_{0i}) + 0.051 (\log_{10}(y_{0i}))^2, \quad (2.18)$$

where y_{0i} is the initial value of y_0 , under the assumption that the equilibrium of $\nu\bar{\nu} \leftrightarrow \chi\bar{\chi}$ is maintained. More specifically,

$$y_{0i} = \lim_{x \rightarrow 0} y_0(x) = \frac{y_0(x)}{B(x)}. \quad (2.19)$$

Combining Eq. (2.19) with Eq. (2.15), we obtain $y/y_{0i} = \bar{n}_\chi/\bar{n}_\nu$. Here \bar{n}_ν could be treated as a constant but the approximation can be further improved by taking into account the increase of \bar{n}_ν due to DM annihilation. More specifically, when χ is in equilibrium with ν , we have $\bar{n}_\chi = \bar{n}_\nu B$. Combining with the conservation of particle number, $N_\nu \bar{n}_\nu + \bar{n}_\chi =$

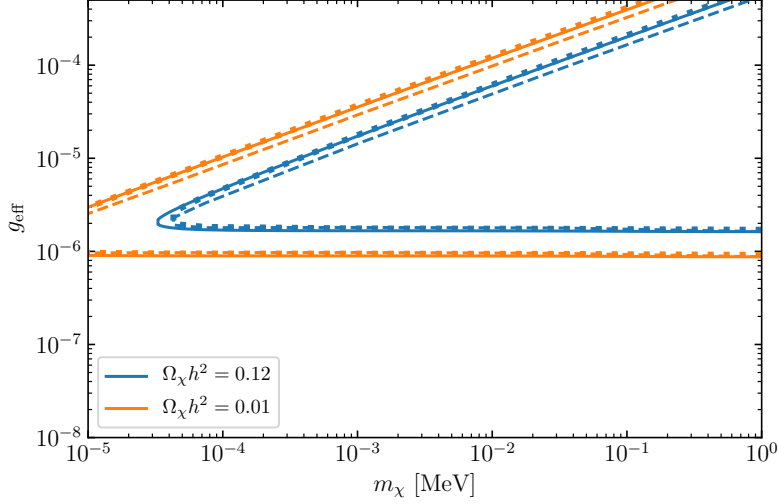


Figure 4. Required DM-neutrino interaction strength to produce the observed DM relic abundance or part of it. The solid curves represent results obtained by the model-independent approach—solving Eq. (2.3) with the parametrization of $\langle\sigma v\rangle$ in Eq. (2.8). Dashed and dotted (almost overlap with the solid) curves represent results obtained by solving the Boltzmann equations for the specific s - and t -channel models, including the complete set of relevant reactions—see Eqs. (2.24)-(2.25).

$N_\nu \bar{n}_\nu^{\text{st}}$ where \bar{n}_ν^{st} stands for the value of \bar{n}_ν in the standard cosmological model, we obtain $\bar{n}_\nu = \frac{N_\nu}{N_\nu + B} \bar{n}_\nu^{\text{st}}$. As B decreases from 1 to a vanishing value, \bar{n}_ν increases from $\bar{n}_\nu \approx \frac{3}{4} \bar{n}_\nu^{\text{st}}$ to $\bar{n}_\nu \approx \bar{n}_\nu^{\text{st}}$. In this way, we obtain the following result:

$$\bar{n}_\chi = \frac{y(x)}{y_{0i}} \frac{N_\nu}{N_\nu + B(x)} \bar{n}_\nu^{\text{st}}, \quad (2.20)$$

where $y(x)$ takes the piecewise function in Eq. (2.17).

In the left panel of Fig. 3, we plot Eq. (2.20) by the orange dash-dotted curve for $m_\chi = 10$ keV, $\Lambda = m_\chi/\sqrt{3}$, and $\langle\sigma v\rangle_0 = 1.6 \times 10^{-21} m_\chi^2$, corresponding to $R_\Lambda = 56.8$. The curve agrees well with the numerical solution in the low- T regime.

In the right panel of Fig. 3, we vary $R_\Lambda \propto \langle\sigma v\rangle_0$ from the strongly-coupled regime ($R_\Lambda \gg 1$) to the weakly-coupled regime ($R_\Lambda \ll 1$) and plot the numerical solutions. The plot shows that, as R_Λ increases, the resulting DM abundance first increases until $R_\Lambda \simeq 1$ and then decreases.

2.5 DM relic abundance

By solving the Boltzmann equation (2.3) with the parametrization of $\langle\sigma v\rangle$ in Eq. (2.8) numerically, we obtain the final value of \bar{n}_χ , which should remain constant until today and can be converted to $\Omega_\chi h^2$ as follows:

$$\Omega_\chi h^2 = 0.12 \times \frac{2m_\chi n_\chi}{\rho_{\text{DM},0}} \bigg|_{\text{today}}, \quad (2.21)$$

where $\rho_{\text{DM},0} = 9.74 \times 10^{-12} \text{ eV}^4$ denotes today's DM energy density. Note that the factor of 2 comes from the degree of freedom of both χ and anti- χ .

We then scan the parameter space to determine the required DM-neutrino interaction strength to produce $\Omega_\chi h^2 = 0.12$. There are three free parameters in our model-independent framework, namely m_χ , $\langle\sigma v\rangle_0$ and Λ . We find that as long as Λ/m_χ is an $\mathcal{O}(1)$ quantity, the result is not sensitive to the specific value of Λ . Hence we fix $\Lambda = m_\chi/\sqrt{3}$ and focus on varying m_χ and $\langle\sigma v\rangle_0$. For the convenience of comparison with specific models, we use the following dimensionless g_{eff} instead of $\langle\sigma v\rangle_0$:

$$g_{\text{eff}} \equiv (32\pi m_\chi^2 \langle\sigma v\rangle_0)^{1/4}. \quad (2.22)$$

According to Eq. (2.11), g_{eff} corresponds to $\sqrt{g_\nu g_\chi}$ or y_χ in the s - and t -channel models, respectively.

In Fig. 4, the blue solid curve is obtained by requiring that (m_χ, g_{eff}) leads to the observed DM relic abundance. In addition to that, we also consider the scenario that χ only accounts for part of the observed amount of DM¹. Hence we plot an orange solid curve corresponding to $\Omega_\chi h^2 = 0.01$.

The upper and lower branches of these curves correspond to the freeze-out and freeze-in regimes, respectively. We find that the two branches can be well fitted by the following expression:

$$g_{\text{eff}} \approx \left(\frac{\Omega_\chi h^2}{0.12}\right)^{\mp\frac{1}{4}} \times \begin{cases} 1.6 \times 10^{-5} \left(\frac{m_\chi}{\text{keV}}\right)^{0.53} & \text{freeze-out regime} \\ 1.8 \times 10^{-6} & \text{freeze-in regime} \end{cases}, \quad (2.23)$$

where \mp takes minus and positive signs for the freeze-out and freeze-in regimes, respectively.

2.6 Model-specific analyses

When considering specific models such as the two in Eqs. (2.9) and (2.10), the DM abundance may also be affected by the presence of the mediator. For instance, in the t -channel model, the mediator ϕ (which we assume is a complex scalar with a dark charge) can be produced via $\nu\bar{\nu} \rightarrow \phi\phi^*$ and subsequently decay to DM via $\phi \rightarrow \chi\nu$. In addition, a $\phi\phi^*$ pair can annihilate to $\chi\bar{\chi}$. For the s -channel model, there are also a few additional processes that need to be taken into account. Overall, there are four processes in each of the two models that can directly or indirectly affect the evolution of DM:

$$s\text{-channel model} : \nu\bar{\nu} \leftrightarrow \phi, \nu\bar{\nu} \leftrightarrow 2\phi, \nu\bar{\nu} \leftrightarrow \chi\bar{\chi}, \chi\bar{\chi} \leftrightarrow 2\phi, \quad (2.24)$$

$$t\text{-channel model} : \phi \leftrightarrow \chi\nu, \nu\bar{\nu} \leftrightarrow \phi\phi^*, \nu\bar{\nu} \leftrightarrow \chi\bar{\chi}, \phi\phi^* \leftrightarrow \chi\bar{\chi}. \quad (2.25)$$

In order to fully take these processes into account, we implement a set of Boltzmann equations for the three coupled species, ν , χ , and ϕ , and solve the equations numerically. The implementation is straightforward, with more details given in Appendix C.

We add the results to Fig. 4, presenting them in dashed and dotted curves for the s - and t -channel models respectively. The mediator mass is set at $m_\phi = 5$ eV (s -channel) and $m_\phi = 1.2m_\chi$ (t -channel) in our calculation.

¹As we will show later, χ behaves as warm dark matter in the freeze-in and part of the freeze-out regimes. A mixture of cold and warm DM is a favored scenario when considering the *small-scale problems* of cold DM.

As is shown in Fig. 4, the results obtained for specific models are approximately the same as the one obtained in the model-independent approach. For different models, the results in terms of g_{eff} may vary by $\sim 20\%$. This meets our expectation since the contribution of additional production channels, if comparable to that of $\nu\bar{\nu} \leftrightarrow \chi\bar{\chi}$, can be absorbed by increasing or decreasing $\langle\sigma v\rangle_0$ by roughly a factor of two, corresponding to a variation of g_{eff} by $2^{1/4} - 1 \approx 20\%$.

It is possible, however, by tuning the couplings and masses such that one of those additional channels dominates significantly over $\nu\bar{\nu} \leftrightarrow \chi\bar{\chi}$. For example, if $g_\chi \gg g_\nu$ in the s -channel model, the relic abundance of χ in the freeze-out regime would mainly depend on $\chi\bar{\chi} \leftrightarrow 2\phi$, assuming ϕ is light. If m_ϕ is heavier than $2m_\chi$, the dominant way of producing χ would be $\nu\bar{\nu} \rightarrow \phi$ followed by $\phi \rightarrow \chi\bar{\chi}$. Such possibilities are beyond the scope of our current framework which aims at a generic analysis based on the minimal set of parameters.

3 Cosmological consequences and constraints

3.1 N_{eff} constraints

As was mentioned in Sec. 1, the conversion between ν and χ could significantly modify the cosmological observable N_{eff} . The effect of χ on N_{eff} is two-fold:

(i) Those χ particles being produced before neutrino decoupling bring additional entropy into the ν - χ sector when neutrinos decouple. If this part of entropy is fully released to neutrinos, it increases N_{eff} .

(ii) After neutrino decoupling, the reaction $\nu\bar{\nu} \rightarrow \chi\bar{\chi}$ consumes decoupled neutrinos and stores a significant amount of entropy into the χ sector. Although a portion of the entropy (depending on how large R_Λ is) will be returned to ν at a later phase, the evolution after neutrino decoupling overall leads to a decrease of N_{eff} .

Therefore, the deviation of N_{eff} from its standard value $N_{\text{eff}}^{\text{st}}$, defined as

$$\Delta N_{\text{eff}} = N_{\text{eff}} - N_{\text{eff}}^{\text{st}}, \quad (3.1)$$

can be positive or negative, depending on whether (i) or (ii) is dominant. Based on the arguments in (i) and (ii), ΔN_{eff} should be positive in the freeze-out regime if g_{eff} is sufficiently large, or negative in the freeze-in regime.

We compute ΔN_{eff} by numerically solving the Boltzmann equations of the ν - χ coupled sector and extracting the final abundance of neutrinos after the freeze-out/in process has completed. The result is presented in Fig. 5, which shows that indeed the resulting ΔN_{eff} is positive for large g_{eff} and it turns negative when g_{eff} is below $\sim 10^{-5}$ (the black solid line). The negative ΔN_{eff} can drop to as low as -0.36 . This could be an interesting observational consequence of our light DM scenario, since many new physics modifications of N_{eff} often leads to positive ΔN_{eff} .

Currently the most precise measurement of N_{eff} comes from Planck 2018 [32], $N_{\text{eff}} = 2.99 \pm 0.17$. Subtracting the standard value $N_{\text{eff}}^{\text{st}} \approx 3.045$ [33–37] from it, we obtain

$$-0.395 < \Delta N_{\text{eff}} < 0.285, \quad (2\sigma \text{ C.L.}). \quad (3.2)$$

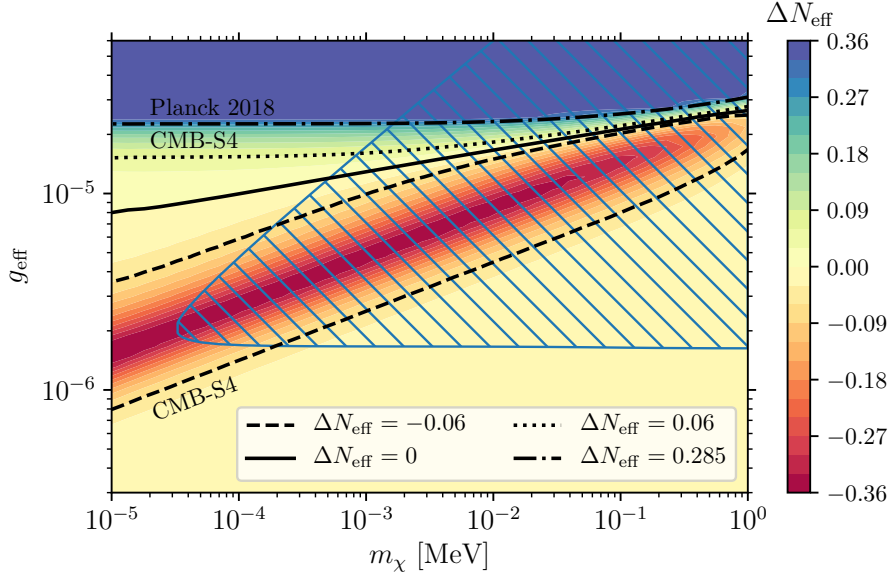


Figure 5. The effect of $\nu\bar{\nu} \leftrightarrow \chi\bar{\chi}$ on ΔN_{eff} . The region below or above the black solid line leads to $\Delta N_{\text{eff}} < 0$ or > 0 , respectively. The hatched region causes an overproduction of DM ($\Omega_\chi h^2 > 0.12$).

We plot the upper bound as a dash-dotted curve in Fig. 5. The lower bound, -0.395 , is not sufficiently constraining to be presented here. Future CMB experiments like Simons Observatory (SO) [38, 39], CMB-S4 [40, 41], and CMB-HD [42] will significantly improve the measurement of ΔN_{eff} , reaching the sensitivity of 0.1, 0.06, and 0.028 at 2σ C.L., respectively. This would allow the negative values of ΔN_{eff} (e.g. the part encompassed by the dashed curve in Fig. 5) to be probed.

3.2 Lyman- α constraint

Light DM with relatively high velocity could lead to significant modifications of the matter power spectrum at small (~ 0.1 Mpc) scales probed by Lyman- α observations [43–48]. Therefore, Lyman- α observations impose important constraints on our framework. While a dedicated study on the Lyman- α constraints can be rather involved, there are simplified approaches that allow for moderately accurate estimates of the Lyman- α constraints — see e.g. [49–51]. Here we derive the Lyman- α constraints by means of the free stream length, which is computed by

$$\lambda_{\text{FS}} = a_0 \int_{t_{\text{dec}}}^{t_0} \frac{v(t)}{a(t)} dt, \quad (3.3)$$

where v is the velocity of a DM particle, t_{dec} denotes the time when DM becomes kinetically decoupled and starts free streaming, t_0 denotes the time of today, and $a_0 = a(t_0)$. Below we set $a_0 = 1$.

When the DM particle starts free streaming, its momentum scales as $p \propto a^{-1}$, implying

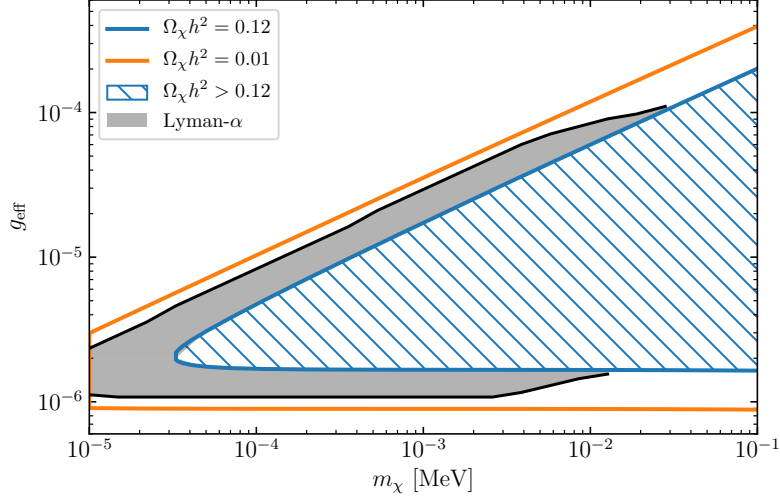


Figure 6. The Lyman- α constraint. The gray region would lead to an overlarge modification of the matter power spectrum at ~ 0.1 Mpc scales and has been ruled out by Lyman- α observations. The hatched region causes an overproduction of DM ($\Omega_\chi h^2 > 0.12$).

that the velocity $v = p/E_p = p/\sqrt{m_\chi^2 + p^2}$ decreases as follows:

$$v = \frac{p_{\text{dec}} a_{\text{dec}} / a}{\sqrt{m_\chi^2 + p_{\text{dec}}^2 a_{\text{dec}}^2 / a^2}}, \quad (3.4)$$

where a_{dec} and p_{dec} denote the values of a and p at kinetic decoupling.

The scale factor varies differently in the radiation-dominated and matter-dominated eras:

$$a = a_{\text{eq}} \left(\frac{t}{t_{\text{eq}}} \right)^\gamma, \quad \gamma = \begin{cases} 1/2 & \text{radiation-dominated} \\ 2/3 & \text{matter-dominated} \end{cases}, \quad (3.5)$$

where a_{eq} and t_{eq} denote the values of a and t at *matter-radiation equality*².

Substituting Eqs. (3.4) and (3.5) into Eq. (3.3), we obtain

$$\lambda_{\text{FS}} = \lambda_{\text{FS, RD}} + \lambda_{\text{FS, MD}}, \quad (3.6)$$

$$\lambda_{\text{FS, RD}} = 2t_{\text{eq}} \frac{\sinh^{-1} \eta_{\text{eq}} - \sinh^{-1} \eta_{\text{dec}}}{a_{\text{eq}} \eta_{\text{eq}}}, \quad (3.7)$$

$$\lambda_{\text{FS, MD}} = \frac{3t_{\text{eq}}}{a_{\text{eq}} \eta_{\text{eq}}}, \quad (3.8)$$

where $\eta \equiv m_\chi/p$, with $\eta_{\text{eq, dec}} = \eta(t = t_{\text{eq, dec}})$. Note that since $\sinh^{-1} \eta \approx \eta$ at $\eta \ll 1$, if $\eta_{\text{dec}} = m_\chi/p_{\text{dec}}$ is sufficiently small (corresponding to sufficiently early decoupling), then $\sinh^{-1} \eta_{\text{dec}}$ in Eq. (3.7) can be omitted, resulting a free-streaming length almost independent of η_{dec} . Eq. (3.8) is derived based on the non-relativistic assumption, as the χ particle should

²Using the Planck 2018 measurements of Λ CDM model parameters [32, 52], we obtain $a_{\text{eq}} = 2.9243 \times 10^{-4}$, corresponding to red-shift $1 + z = 3419.63$ and $T_\gamma = 0.803$ eV.

already be non-relativistic at $t = t_{\text{eq}}$. In Eq. (3.7), we do not require it to be non-relativistic. In fact, it is possible that χ transitions from relativistic to non-relativistic regimes within the range covered by Eq. (3.7). If we replace Eq. (3.4) with a step function that equals to 1 or $v_{\text{eq}} a_{\text{eq}}/a$ in the relativistic and non-relativistic regimes respectively, the above calculation reproduces Eq. (38) in Ref. [51]. As we have checked, the numerical difference between these two approaches is only around 10%.

To estimate the mean value of λ_{FS} , we need to compute the mean value of p :

$$\langle p \rangle \equiv \frac{\int p f_{\chi}(p) d^3 p}{\int f_{\chi}(p) d^3 p}. \quad (3.9)$$

When f_{χ} is in kinetic equilibrium, Eq. (3.9) gives

$$\frac{\langle p \rangle}{T} = \frac{2e^{-x}(x^2 + 3x + 3)}{x^2 K_2(x)} \approx \begin{cases} 2\sqrt{\frac{2}{\pi}}x \approx 1.6\sqrt{x} & \text{non-relativistic} \\ 3 & \text{relativistic} \end{cases}. \quad (3.10)$$

We use Eq. (3.10) to obtain the value of p_{dec} which is then used to compute the mean value of λ_{FS} . By matching the obtained λ_{FS} with the free-streaming length derived from Fig. 6 of Ref. [45] (see also [49] for further interpretations), we can recast the Lyman- α constraint reported in Ref. [45] to the constraint on our model. The result is presented as the gray region in Fig. 6.

3.3 Distortion of $C\nu B$

As mentioned in Sec. 1, after neutrinos have kinetically decoupled from χ , the process $\chi\bar{\chi} \rightarrow \nu\bar{\nu}$ which continues until today (though at a very low rate) may lead to a significant distortion of f_{ν} . The resulting distortion of f_{ν} cannot be washed out if it is produced after neutrinos have started free-streaming.

Before quantitative calculations, we shall clarify the difference between the following two quantities:

$$\tau_{\nu} = \frac{1}{\langle \sigma v \rangle_{\nu\chi \rightarrow \nu\chi} n_{\chi}}, \quad \tau_{\chi} = \frac{1}{\langle \sigma v \rangle_{\nu\chi \rightarrow \nu\chi} n_{\nu}}, \quad (3.11)$$

where $\langle \sigma v \rangle_{\nu\chi \rightarrow \nu\chi}$ denotes the thermally-averaged cross section of $\nu\chi \rightarrow \nu\chi$. Physically, we interpret τ_{ν} as the mean free time (or mean free path, which is equivalent for relativistic species) of a neutrino scattering off a χ particle, and τ_{χ} as the mean free time of a χ particle scattering off a neutrino. Obviously, when $n_{\nu} \gg n_{\chi}$, we have $\tau_{\nu} \gg \tau_{\chi}$, implying that neutrinos can start free-streaming much earlier than χ . This is also quite intuitive—when χ particles are very scarce in the universe, it is much more difficult for a neutrino to find a χ particle to collide with than a χ particle to find a neutrino to collide with.

Therefore, when the terminology *kinetic decoupling* is used, one should distinguish between the kinetic decoupling of ν from χ and that of χ from ν . The former happens when τ_{ν} starts to exceed H^{-1} , meaning that the time it would take for a neutrino to find a χ particle is longer than the Hubble time. Likewise, the kinetic decoupling of χ from ν occurs when $\tau_{\chi} \gtrsim H^{-1}$.

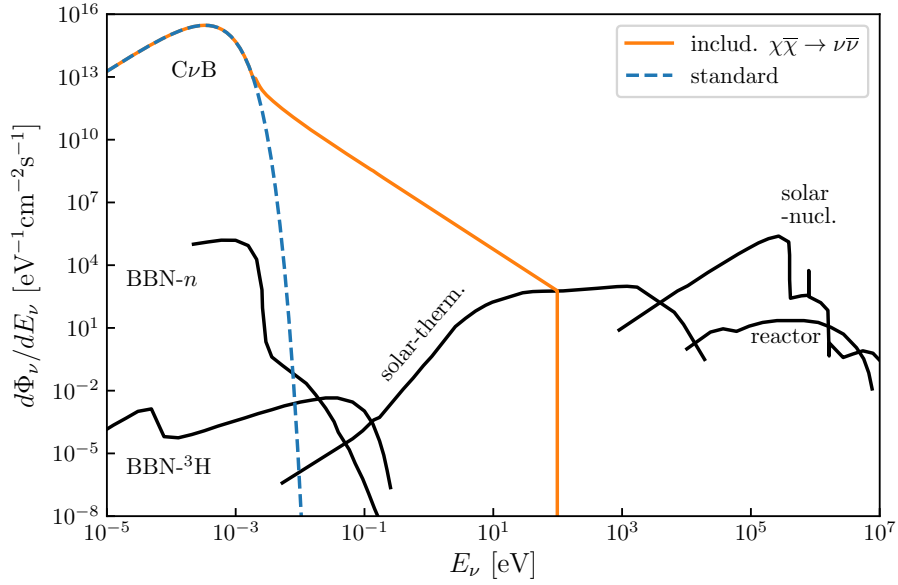


Figure 7. The impact of DM annihilation on CνB. The black curves represent other known neutrino fluxes at low energies, including those from BBN- n and BBN- ^3H decays, solar thermal (solar-therm.) and nuclear (solar-nucl.) reactions and reactors, taken from [53].

To compute the distortion, we adopt the Boltzmann equation of f_ν and focus only on the period when $\tau_\nu \gtrsim H^{-1}$. The Boltzmann equation reads:

$$\left[\frac{\partial}{\partial t} - H p \frac{\partial}{\partial p} \right] f_\nu(p, t) = C^{(f)}, \quad (3.12)$$

where the collision term $C^{(f)}$ is given as follows:

$$C^{(f)} = \frac{2\pi^2}{m_\chi^2} n_\chi^2 \langle \sigma v \rangle_0 \delta(p - m_\chi). \quad (3.13)$$

Note that when integrating over p , it reproduces the collision term for n_ν :

$$\int C^{(f)} \frac{d^3 p}{(2\pi)^3} = n_\chi^2 \langle \sigma v \rangle_0. \quad (3.14)$$

The Boltzmann equation can be analytically solved by means of variable transformation $(t, p) \rightarrow (a, x_p)$ with $x_p \equiv p/T$ —see Appendix B in Ref. [10] for further details. Using this method, the correction to f_ν caused by $\chi\bar{\chi} \rightarrow \nu\bar{\nu}$ at $\tau_\nu \gtrsim H^{-1}$ can be computed by

$$\delta f_\nu = \int_{a_{\nu\text{FS}}}^{a_0} \frac{C^{(f)}(a, x_p)}{H a} da = \frac{2\pi^2 n_\chi^2}{H_m m_\chi^2} \langle \sigma v \rangle_0 x_p^2 \Theta, \quad (3.15)$$

where $a_{\nu\text{FS}}$ denotes the scale factor when ν starts free-streaming, and $\Theta = 1$ if $x_p^{\min} < x_p < x_p^{\max}$ or 0 if x_p is not in this range. The minimum and maximum of x_p are determined by requiring that $\int_{a_{\nu\text{FS}}}^{a_0} \delta(x_p T - m_\chi) da$ is nonzero. Note that here and also in Eq. (3.15), x_p

is treated as an a -independent variable, while $T \propto a^{-1}$ is a -dependent. The maximum of x_p corresponds to DM annihilation today which produces ν without red-shift, while earlier production of ν is subjected to higher red-shift. Hence the maximum is given by $x_p^{\max} = m_\chi/T_0$ where T_0 denotes the value of T today (approximately the neutrino temperature today), and the minimum is given by $x_p^{\min} = a_{\nu\text{FS}}x_p^{\max}$ which is a red-shifted value of x_p^{\max} .

Here we should clarify a subtle difference between the number density n_χ in Eq. (3.14) and the n_χ in Eq. (3.15). The former varies in time, while the latter is no longer time-dependent after integrating over a , essentially equivalent to integrating over time. The former n_χ is actually a function of a while the latter n_χ should be a function of x_p . By checking how the Dirac delta function is integrated out, we can see that the latter n_χ is the number density of χ at $x_p = ax_p^{\max}$. Consequently, the dependence of the former n_χ on a transforms into the dependence of the latter n_χ on x_p via $n_\chi = n_\chi|_{a \rightarrow x_p/x_p^{\max}}$.

Let us consider a specific benchmark as a case study. It is based on the t -channel model, with the following input parameters:

$$y = 10^{-5}, \quad m_\chi = 0.1 \text{ keV}, \quad m_\phi/m_\chi = 1.2. \quad (3.16)$$

The thermally-averaged cross section of $\nu\chi \rightarrow \nu\chi$ in the t -channel model is given by

$$\langle\sigma v\rangle_{\nu\chi \rightarrow \nu\chi} \approx \frac{3T^2 y^4}{\pi (m_\phi^2 - m_\chi^2)^2}, \quad (\text{for } T \ll m_\phi - m_\chi), \quad (3.17)$$

where we have made non-relativistic approximation of χ and taken the low- T limit.

Using Eq. (3.17) and Eq. (3.11), we obtain

$$\frac{\tau_\nu}{H^{-1}} \approx \frac{1.0 \text{ eV}^3}{n_\chi} \left(\frac{m_\chi}{0.1 \text{ keV}} \right)^4 \cdot \left(\frac{10^{-5}}{y} \right)^4. \quad (3.18)$$

This ratio would exceed 1 when n_χ is below 1eV^3 for the given benchmark. According to the numerical solution, this occurs when $x = m_\chi/T$ arrives at

$$x_{\nu\text{FS}} \approx 12.6. \quad (3.19)$$

It is also straightforward to obtain the freeze-out value for this benchmark, $x_{\text{f.o}} \approx 5.0$. By comparing the two values, one can see that neutrinos start free-streaming later than freeze-out.

It is straightforward to evaluate the quantities in Eq. (3.15) for the above benchmark and obtain the distortion of C ν B, which is presented in Fig. 7. Here the y -axis is presented in terms of the neutrino differential flux $d\Phi_\nu/dE_\nu$, which for the isotropic and homogeneous C ν B is related to f_ν by $d\Phi_\nu/dE_\nu = p^2 f_\nu/(2\pi^2)$. According to Eq. (3.15), the flux generated by DM annihilation is $d\Phi_\nu/dE_\nu \propto p^2 n_\chi^2 x_p^2 \propto E_\nu^{-2}$. Therefore, the high-energy tail of the C ν B spectrum is altered from exponential suppression to E_ν^{-2} , substantially enhancing the C ν B flux at high energies.

It is particularly interesting to note that the enhanced C ν B tail would entirely change the landscape of existing neutrino spectra in the sub-eV to keV range, in which the only

known neutrino sources in addition to $C\nu B$ are neutron (n) and tritium (${}^3\text{H}$) decays during BBN and solar thermal neutrinos [53]. Their fluxes are well below the orange curve for $E_\nu \leq m_\chi$. If future experiments are capable to detect neutrinos within the eV-keV range, the altered $C\nu B$ tail would be the most predominant signal in this energy range. In particular, for $C\nu B$ detection experiments such as PTOLEMY [54, 55], in which the primary challenge lies in sub-eV energy measurements [56, 57], the distorted $C\nu B$ in our framework offers a technically more accessible scenario to probe.

4 Summary and conclusions

A dark sector interacting with the SM via the neutrino portal is one of the most appealing scenarios discussed in the literature. Such interactions can not only be responsible for the thermal production of dark matter (DM) but also leave cosmological imprints at various stages of the early universe.

In this paper, we systematically investigate a generic framework in which DM interacts with neutrinos, and the interaction strength can be effectively quantified by the thermally-averaged cross section $\langle\sigma v\rangle$. We propose a model-independent parametrization of $\langle\sigma v\rangle$ and demonstrate that it can accurately account for the production and annihilation rates of DM across a wide range of temperatures, applicable to both relativistic and non-relativistic DM particles. By feeding the parametrized $\langle\sigma v\rangle$ into the Boltzmann equation, we solve the Boltzmann equation and obtain the DM relic abundance for a broad range of parameter space. When specific models are considered, the results are approximately the same as those obtained in our model-independent approach, as shown in Figs. 2 and 4. Moreover, our parametrized $\langle\sigma v\rangle$ allows the thermal evolution of DM to be computed analytically, with the analytic result agreeing well with the numerical one.

The interplay between DM with neutrinos may result in interesting cosmological imprints on neutrinos. We show that N_{eff} can be modified significantly due to DM production and annihilation. A particularly noteworthy feature here is that large negative ΔN_{eff} (e.g. -0.36) is possible and lies slightly beyond the reach of the Planck 2018 measurement. Future experiments such as CMB-S4 are capable to probe this interesting deviation. Furthermore, DM annihilation at late times after kinetic decoupling might distort the $C\nu B$ energy spectrum, yielding a substantially enhanced $C\nu B$ tail with the neutrino flux much higher than that from BBN isotope decays and solar thermal neutrinos—see Fig. 7. Such an enhancement would have great implications for future $C\nu B$ detection experiments.

Acknowledgments

We thank Laura Lopez-Honorez and Keisuke Harigaya for useful discussions. Fermilab is operated by Fermi Research Alliance, LLC under Contract No. DE-AC02-07CH11359 with the U.S. Department of Energy, Office of Science, Office of High Energy Physics. I.R.W. is supported by DOE distinguished scientist fellowship grant FNAL 22-33. I.R.W. was supported by DOE-SC0010008 when at Rutgers at the early stage of this work. The work of X.J.X is supported in part by the National Natural Science Foundation of China under

grant No. 12141501 and also by the CAS Project for Young Scientists in Basic Research (YSBR-099). X.J.X would also like to thank the Hangzhou Institute for Advanced Study (HIAS) for the hospitality during his visit when this work was performed in part.

A Collision terms and thermally-averaged cross sections

The Boltzmann equation in Eq. (2.3) in terms of $\langle\sigma v\rangle$ is derived from the following form

$$\frac{dn_\chi}{dt} + 3Hn_\chi = -N_\nu C_{\chi\bar{\chi}\leftrightarrow\nu\bar{\nu}}, \quad (\text{A.1})$$

where

$$C_{\chi\bar{\chi}\leftrightarrow\nu\bar{\nu}} \equiv \int [f_\chi(p_1)f_{\bar{\chi}}(p_2) - f_\nu(p_3)f_{\bar{\nu}}(p_4)] |\mathcal{M}|^2 (2\pi\delta)^4 d\Pi_1 d\Pi_2 d\Pi_3 d\Pi_4. \quad (\text{A.2})$$

Due to kinetic equilibrium [see Eq. (2.1)], $\langle\sigma v\rangle$ can be equivalently given by the following four different forms:

$$\langle\sigma v\rangle = n_\chi^{-2} \int f_\chi(p_1)f_\chi(p_2) |\mathcal{M}|^2 (2\pi\delta)^4 d\Pi_1 d\Pi_2 d\Pi_3 d\Pi_4 \quad (\text{A.3})$$

$$= (n_\chi^{\text{eq}})^{-2} \int f_\chi^{\text{eq}}(p_1)f_\chi^{\text{eq}}(p_2) |\mathcal{M}|^2 (2\pi\delta)^4 d\Pi_1 d\Pi_2 d\Pi_3 d\Pi_4 \quad (\text{A.4})$$

$$= (n_\chi^{\text{eq}})^{-2} \int f_\nu^{\text{eq}}(p_3)f_\nu^{\text{eq}}(p_4) |\mathcal{M}|^2 (2\pi\delta)^4 d\Pi_1 d\Pi_2 d\Pi_3 d\Pi_4 \quad (\text{A.5})$$

$$= \left(\frac{n_\nu^{\text{eq}}}{n_\chi^{\text{eq}}}\right)^2 \frac{1}{n_\nu^2} \int f_\nu(p_3)f_\nu(p_4) |\mathcal{M}|^2 (2\pi\delta)^4 d\Pi_1 d\Pi_2 d\Pi_3 d\Pi_4. \quad (\text{A.6})$$

Note that from Eq. (A.4) to Eq. (A.5), the δ function allows the replacement $f_\chi^{\text{eq}}(p_1)f_\chi^{\text{eq}}(p_2) = e^{-(E_1+E_2)/T} \rightarrow f_\nu^{\text{eq}}(p_3)f_\nu^{\text{eq}}(p_4) = e^{-(E_3+E_4)/T}$.

Applying Eqs. (A.3) and (A.6) to Eq. (A.2), we obtain

$$\frac{dn_\chi}{dt} + 3Hn_\chi = -N_\nu \langle\sigma v\rangle \left[n_\chi^2 - \left(\frac{n_\chi^{\text{eq}}}{n_\nu^{\text{eq}}}\right)^2 n_\nu^2 \right], \quad (\text{A.7})$$

which is essentially Eq. (2.3).

For other two-to-two processes we have encountered in this work such as $2\phi \rightarrow 2\chi$, one can obtain similar equations, independent of whether the initial and final states are massless or not.

The collision term $C_{\chi\bar{\chi}\leftrightarrow\nu\bar{\nu}}$ in Eq. (A.2) can be split into two terms

$$C_{\chi\bar{\chi}\leftrightarrow\nu\bar{\nu}} = C_{\chi\bar{\chi}\rightarrow\nu\bar{\nu}} - C_{\nu\bar{\nu}\rightarrow\chi\bar{\chi}}, \quad (\text{A.8})$$

where $C_{\chi\bar{\chi}\rightarrow\nu\bar{\nu}}$ and $C_{\nu\bar{\nu}\rightarrow\chi\bar{\chi}}$ correspond to the integral in Eq. (A.2) with $[f_\chi f_{\bar{\chi}} - f_\nu f_{\bar{\nu}}]$ replaced by $f_\chi f_{\bar{\chi}}$ and $f_\nu f_{\bar{\nu}}$, respectively. From Eq. (2.6), we have

$$\langle\sigma v\rangle = \frac{1}{n_\chi^2} C_{\chi\bar{\chi}\rightarrow\nu\bar{\nu}} = \left(\frac{n_\nu^{\text{eq}}}{n_\chi^{\text{eq}}}\right)^2 \frac{1}{n_\nu^2} C_{\nu\bar{\nu}\rightarrow\chi\bar{\chi}}. \quad (\text{A.9})$$

The collision terms $C_{\chi\bar{\chi}\rightarrow\nu\bar{\nu}}$ and $C_{\nu\bar{\nu}\rightarrow\chi\bar{\chi}}$ can be computed by integrating the cross sections of their respective processes — see Ref. [31]. Specifically, assuming $f_{\nu(\bar{\nu})}(p) = e^{-p/T}$ or $f_{\chi(\bar{\chi})}(p) = e^{-E_p/T}$ with $E_p = \sqrt{m_\chi^2 + p^2}$, we have

$$C_{\nu\bar{\nu}\rightarrow\chi\bar{\chi}} = \frac{T}{32\pi^4} \int_{4m_\chi^2}^{\infty} s^{3/2} \sigma_{\nu\bar{\nu}\rightarrow\chi\bar{\chi}} K_1\left(\frac{s^{1/2}}{T}\right) ds, \quad (\text{A.10})$$

$$C_{\chi\bar{\chi}\rightarrow\nu\bar{\nu}} = \frac{T}{32\pi^4} \int_{4m_\chi^2}^{\infty} s^{1/2} (s - 4m_\chi^2) \sigma_{\chi\bar{\chi}\rightarrow\nu\bar{\nu}} K_1\left(\frac{s^{1/2}}{T}\right) ds. \quad (\text{A.11})$$

If ν or χ are not in chemical equilibrium but in kinetic equilibrium, Eqs. (A.10) and (A.11) are changed by a factor of $(n_\nu/n_\nu^{\text{eq}})^2$ or $(n_\chi/n_\chi^{\text{eq}})^2$. Either Eq. (A.10) or Eq. (A.11) can be used to compute $\langle\sigma v\rangle$ in Eq. (A.9), and would lead to the same result.

For the specific s - and t -channel models introduced in Eqs. (2.9) and (2.10), the cross sections are given by³ [8]

$$\sigma_{\nu\bar{\nu}\rightarrow\chi\bar{\chi}}^{(s)} = \frac{g_\chi^2 g_\nu^2}{12\pi} \frac{s - m_\chi^2}{(s - m_\phi^2)^2} \Delta, \quad (\text{A.12})$$

$$\sigma_{\nu\bar{\nu}\rightarrow\chi\bar{\chi}}^{(t)} = \frac{y_\chi^4}{16\pi s^2} \left[\frac{sm_\phi^2 + 2\delta^4}{sm_\phi^2 + \delta^4} s\Delta + 2\delta^2 \log\left(\frac{1 - \Delta + 2\delta^2/s}{1 + \Delta + 2\delta^2/s}\right) \right], \quad (\text{A.13})$$

with

$$\Delta \equiv \sqrt{1 - \frac{4m_\chi^2}{s}}, \quad \delta^2 \equiv m_\phi^2 - m_\chi^2. \quad (\text{A.14})$$

For analytical calculations, it is useful to mention the following limits

$$\lim_{\delta\rightarrow 0} \sigma_{\nu\bar{\nu}\rightarrow\chi\bar{\chi}}^{(t)} = \frac{y_\chi^4}{16\pi s} \Delta, \quad \lim_{m_\phi\rightarrow 0} \sigma_{\nu\bar{\nu}\rightarrow\chi\bar{\chi}}^{(s)} = \frac{g_\chi^2 g_\nu^2}{12\pi s} \left(1 - \frac{m_\chi^2}{s}\right) \Delta. \quad (\text{A.15})$$

With the cross sections in Eq. (A.15), $\langle\sigma v\rangle$ can be computed analytically in the low- T and high- T limits.

In the low- T limit, assuming $x = m_\chi/T \gg 1$, we obtain

$$\langle\sigma v\rangle^{(t)} = \frac{y_\chi^4}{32\pi m_\chi^2} [1 - 3x^{-1} + \mathcal{O}(x^{-2})], \quad (\text{A.16})$$

$$\langle\sigma v\rangle^{(s)} = \frac{g_\chi^2 g_\nu^2}{32\pi m_\chi^2} \left[1 - \frac{5}{2}x^{-1} + \mathcal{O}(x^{-2})\right]. \quad (\text{A.17})$$

In the high- T limit, assuming $x = m_\chi/T \ll 1$, we obtain

$$\langle\sigma v\rangle^{(t)} = \frac{y_\chi^4}{128\pi T^2} + \mathcal{O}(x^2), \quad (\text{A.18})$$

$$\langle\sigma v\rangle^{(s)} = \frac{g_\chi^2 g_\nu^2}{96\pi T^2} + \mathcal{O}(x^2). \quad (\text{A.19})$$

³Computations for the cross sections are cross-checked in this work under the help of FEYNCALC 9.3.0 [58–60] and PACKAGE-X [61, 62].

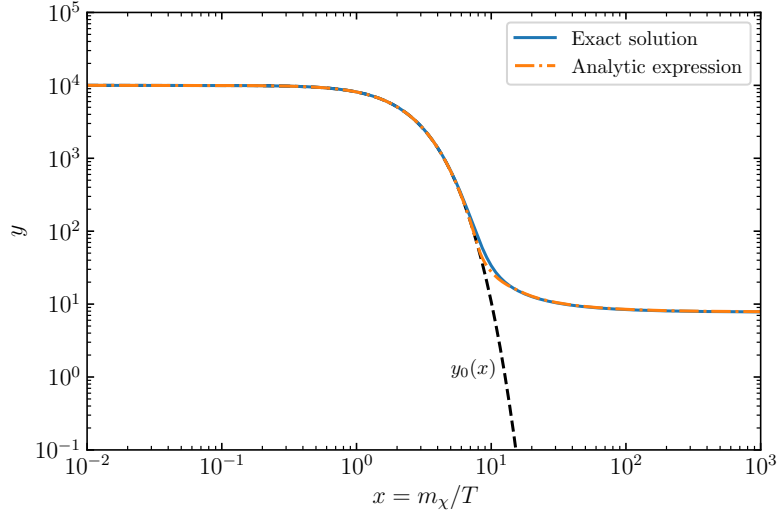


Figure 8. Comparison of the analytical expression in Eq. (B.5) with the exact solution obtained by numerically solving Eq. (B.1) with $R = 10^4$.

For general values of T (e.g. for the solid curves in Fig. 2), we compute the integral in Eq. (A.10) numerically to obtain $C_{\nu\bar{\nu}\rightarrow\chi\bar{\chi}}$ and hence $\langle\sigma v\rangle$.

B Useful approximations in the freeze-out regime

The Boltzmann equation in the freeze-out regime can be reformulated into the following form which is essentially a Riccati equation:

$$y'(x) = -\frac{y(x)^2 - y_0(x)^2}{x^2}, \quad (\text{B.1})$$

with

$$y_0(x) = R \frac{x^2 K_2(x)}{2} \approx R \times \begin{cases} 1 & \text{for } x \ll 1 \\ \frac{1}{2} \sqrt{\frac{\pi}{2}} x^{3/2} e^{-x} & \text{for } x \gg 1 \end{cases}. \quad (\text{B.2})$$

Eq. (B.1) in general cannot be solved analytically. But in the limit of vanishing y_0 it has the following solution

$$y = \frac{x}{x/y_\infty - 1}, \quad (y_0 \rightarrow 0), \quad (\text{B.3})$$

where y_∞ denotes the value of y at $x \rightarrow \infty$. The solution is divergent at $x = y_\infty$, which implies that it is invalid when x is below y_∞ . Therefore, the freeze-out value of x is approximately given by

$$x_{\text{f.o.}} \approx y_\infty. \quad (\text{B.4})$$

For $x \ll x_{\text{f.o.}}$, χ should be in equilibrium, implying that the solution is approximately given by the equilibrium value, $y(x) \approx y_0(x)$. Combining this and Eq. (B.3), we obtain the

following analytical solution:

$$y = \begin{cases} \frac{x}{x/x_{f.o}-1} & x > 2x_{f.o} \\ y_0(x) & x < x_{f.o} \\ \frac{x y_{f.o}}{x(\xi-1)+x_{f.o}(2-\xi)} & x \in [x_{f.o}, 2x_{f.o}] \end{cases}, \quad (\text{B.5})$$

where $y_{f.o} \equiv y_0(x_{f.o})$ and $\xi \equiv y_{f.o}/x_{f.o}$. Here we assume a transition interval $[x_{f.o}, 2x_{f.o}]$. Within this interval, the solution is obtained by assuming an expression of the form $x/(ax+b)$ with a and b determined by the continuity of the solution.

In Fig. 8, we show that Eq. (B.5) as an approximate solution is very close to the exact one. However, we should note that in the use of Eq. (B.5) one has to determine $x_{f.o}$ accurately. This could be obtained from the widely used criteria that $x_{f.o}$ corresponds to $n_\chi \langle \sigma v \rangle_0 \sim H$. A more accurate result can be obtained by numerically solving Eq. (B.1) with various given values of R and then performing a polynomial (in terms of $\log_{10} R$) fit to the results. In this way, we find

$$x_{f.o} \approx 0.048 + 1.73 \log_{10} R + 0.051 (\log_{10} R)^2, \quad (\text{B.6})$$

which serves as a formula for computing $x_{f.o}$ with precision at the percent level.

C Solving Boltzmann equations for three coupled species

In Sec. 2.6, we computed the DM relic abundance for the specific s - and t -channel models. This requires solving the Boltzmann equations for three coupled species:

$$\frac{dn_i}{dt} + 3Hn_i = C_{\text{prod.}}^{(n_i)} - C_{\text{depl.}}^{(n_i)}, \quad (i = \nu, \chi, \phi). \quad (\text{C.1})$$

where $C_{\text{prod.}}^{(n_i)}$ and $C_{\text{depl.}}^{(n_i)}$ denote the collision terms accounting for the production and the depletion of n_i . In our numerical code, we solve the Boltzmann equations by reformulating them into the following form

$$\frac{d(n_i a^3)}{da} = \frac{a^2}{H} [C_{\text{prod.}}^{(n_i)} - C_{\text{depl.}}^{(n_i)}]. \quad (\text{C.2})$$

According to Eq. (2.24), the collision terms for the s -channel model include the following contributions:

$$C_{\text{prod.}}^{(n_\nu)} = N_\phi C_{\phi \rightarrow \nu \bar{\nu}} + N_\phi C_{2\phi \rightarrow \nu \bar{\nu}} + C_{\chi \bar{\chi} \rightarrow \nu \bar{\nu}}, \quad (\text{C.3})$$

$$C_{\text{depl.}}^{(n_\nu)} = N_\phi C_{\nu \bar{\nu} \rightarrow \phi} + N_\phi C_{\nu \bar{\nu} \rightarrow 2\phi} + C_{\nu \bar{\nu} \rightarrow \chi \bar{\chi}}, \quad (\text{C.4})$$

$$C_{\text{prod.}}^{(n_\chi)} = N_\phi C_{2\phi \rightarrow \chi \bar{\chi}} + N_\nu C_{\nu \bar{\nu} \rightarrow \chi \bar{\chi}}, \quad (\text{C.5})$$

$$C_{\text{depl.}}^{(n_\chi)} = N_\phi C_{\chi \bar{\chi} \rightarrow 2\phi} + N_\nu C_{\chi \bar{\chi} \rightarrow \nu \bar{\nu}}, \quad (\text{C.6})$$

$$C_{\text{prod.}}^{(n_\phi)} = N_\nu C_{\phi \rightarrow \nu \bar{\nu}} + 2N_\nu C_{\nu \bar{\nu} \rightarrow 2\phi} + 2C_{\chi \bar{\chi} \rightarrow 2\phi}, \quad (\text{C.7})$$

$$C_{\text{depl.}}^{(n_\phi)} = N_\nu C_{\nu \bar{\nu} \rightarrow \phi} + 2N_\nu C_{2\phi \rightarrow \nu \bar{\nu}} + 2C_{2\phi \rightarrow \chi \bar{\chi}}, \quad (\text{C.8})$$

where $N_\phi = 3$ accounts for the three polarization modes of the vector ϕ .

It is worth mentioning a few consistency checks for the coefficients in Eqs. (C.3)-(C.8). When combining the Boltzmann equations of two species together, there should be some kind of cancellations among the right-hand sides of the Boltzmann equations. For instance, if only $\phi \leftrightarrow \nu\bar{\nu}$ is present, then we expect that the total number of ϕ and ν in a comoving volume is conserved, i.e. $d[(N_\nu n_\nu + N_\phi n_\phi)a^3]/da = 0$. Indeed, one can see that the combination [Eq. (C.3)-Eq. (C.4)] $\times N_\nu$ + [Eq. (C.7)-Eq. (C.8)] $\times N_\phi$ vanishes if only $\phi \leftrightarrow \nu\bar{\nu}$ is present. Similar consistency checks also apply to other terms. Specifically, when only $2\phi \leftrightarrow \nu\bar{\nu}$, $\chi\bar{\chi} \leftrightarrow \nu\bar{\nu}$ or $\chi\bar{\chi} \leftrightarrow 2\phi$ is present, then $(2N_\nu n_\nu + N_\phi n_\phi)a^3$, $(N_\nu n_\nu + n_\chi)a^3$ or $(2n_\chi + N_\phi n_\phi)a^3$ is conserved, respectively.

For the t -channel model, Eqs. (C.3)-(C.8) should be changed to the following forms:

$$C_{\text{prod.}}^{(n_\nu)} = C_{\phi \rightarrow \chi\nu} + C_{\phi\phi^* \rightarrow \nu\bar{\nu}} + C_{\chi\bar{\chi} \rightarrow \nu\bar{\nu}}, \quad (\text{C.9})$$

$$C_{\text{depl.}}^{(n_\nu)} = C_{\chi\nu \rightarrow \phi} + C_{\nu\bar{\nu} \rightarrow \phi\phi^*} + C_{\nu\bar{\nu} \rightarrow \chi\bar{\chi}}, \quad (\text{C.10})$$

$$C_{\text{prod.}}^{(n_\chi)} = C_{\phi\phi^* \rightarrow \chi\bar{\chi}} + N_\nu C_{\nu\bar{\nu} \rightarrow \chi\bar{\chi}}, \quad (\text{C.11})$$

$$C_{\text{depl.}}^{(n_\chi)} = C_{\chi\bar{\chi} \rightarrow \phi\phi^*} + N_\nu C_{\chi\bar{\chi} \rightarrow \nu\bar{\nu}}, \quad (\text{C.12})$$

$$C_{\text{prod.}}^{(n_{Z'})} = N_\nu C_{\chi\nu \rightarrow \phi} + N_\nu C_{\nu\bar{\nu} \rightarrow \phi\phi^*} + C_{\chi\bar{\chi} \rightarrow \phi\phi^*}, \quad (\text{C.13})$$

$$C_{\text{depl.}}^{(n_{Z'})} = N_\nu C_{\phi \rightarrow \chi\nu} + N_\nu C_{\phi\phi^* \rightarrow \nu\bar{\nu}} + C_{\phi\phi^* \rightarrow \chi\bar{\chi}}. \quad (\text{C.14})$$

Again, one can check that there are similar cancellations among the collision terms to guarantee that some combinations of particle numbers are conserved.

References

- [1] A. Falkowski, J. Juknevič, and J. Shelton, *Dark matter through the neutrino portal*, [0908.1790](#).
- [2] V. González-Macías, J. I. Illana, and J. Wudka, *A realistic model for dark matter interactions in the neutrino portal paradigm*, *JHEP* **05** (2016) 171, [[1601.05051](#)].
- [3] M. Escudero, N. Rius, and V. Sanz, *Sterile neutrino portal to dark matter i: The $u(1)_{B-L}$ case*, *JHEP* **02** (2017) 045, [[1606.01258](#)].
- [4] M. Escudero, N. Rius, and V. Sanz, *Sterile neutrino portal to dark matter ii: Exact dark symmetry*, *Eur. Phys. J. C* **77** (2017), no. 6 397, [[1607.02373](#)].
- [5] B. Batell, T. Han, and B. Shams Es Haghi, *Indirect detection of neutrino portal dark matter*, *Phys. Rev. D* **97** (2018), no. 9 095020, [[1704.08708](#)].
- [6] M. Becker, *Dark matter from freeze-in via the neutrino portal*, *Eur. Phys. J. C* **79** (2019), no. 7 611, [[1806.08579](#)].
- [7] M. Blennow, E. Fernandez-Martinez, A. Olivares-Del Campo, S. Pascoli, S. Rosauero-Alcaraz, and A. V. Titov, *Neutrino portals to dark matter*, *Eur. Phys. J. C* **79** (2019), no. 7 555, [[1903.00006](#)].

- [8] M. Hufnagel and X.-J. Xu, *Dark matter produced from neutrinos*, *JCAP* **01** (2022), no. 01 043, [[2110.09883](#)].
- [9] B. Barman, P. S. Bhupal Dev, and A. Ghoshal, *Probing freeze-in dark matter via heavy neutrino portal*, *Phys. Rev. D* **108** (2023), no. 3 035037, [[2210.07739](#)].
- [10] S.-P. Li and X.-J. Xu, *Dark matter produced from right-handed neutrinos*, *JCAP* **06** (2023) 047, [[2212.09109](#)].
- [11] X.-J. Xu, S. Zhou, and J. Zhu, *The ν_R -philic scalar dark matter*, [2310.16346](#).
- [12] P. Serra, F. Zalamea, A. Cooray, G. Mangano, and A. Melchiorri, *Constraints on neutrino – dark matter interactions from cosmic microwave background and large scale structure data*, *Phys. Rev. D* **81** (2010) 043507, [[0911.4411](#)].
- [13] R. J. Wilkinson, C. Boehm, and J. Lesgourgues, *Constraining Dark Matter-Neutrino Interactions using the CMB and Large-Scale Structure*, *JCAP* **05** (2014) 011, [[1401.7597](#)].
- [14] N. Becker, D. C. Hooper, F. Kahlhoefer, J. Lesgourgues, and N. Schöneberg, *Cosmological constraints on multi-interacting dark matter*, *JCAP* **02** (2021) 019, [[2010.04074](#)].
- [15] M. R. Mosbech, C. Boehm, S. Hannestad, O. Mena, J. Stadler, and Y. Y. Y. Wong, *The full Boltzmann hierarchy for dark matter-massive neutrino interactions*, *JCAP* **03** (2021) 066, [[2011.04206](#)].
- [16] P. F. Depta, M. Hufnagel, K. Schmidt-Hoberg, and S. Wild, *BBN constraints on the annihilation of MeV-scale dark matter*, *JCAP* **04** (2019) 029, [[1901.06944](#)].
- [17] N. Sabti, J. Alvey, M. Escudero, M. Fairbairn, and D. Blas, *Refined Bounds on MeV-scale Thermal Dark Sectors from BBN and the CMB*, *JCAP* **01** (2020) 004, [[1910.01649](#)].
- [18] G. Mangano, A. Melchiorri, P. Serra, A. Cooray, and M. Kamionkowski, *Cosmological bounds on dark matter-neutrino interactions*, *Phys. Rev. D* **74** (2006) 043517, [[astro-ph/0606190](#)].
- [19] B. Bertoni, S. Ipek, D. McKeen, and A. E. Nelson, *Constraints and consequences of reducing small scale structure via large dark matter-neutrino interactions*, *JHEP* **04** (2015) 170, [[1412.3113](#)].
- [20] L. J. Hall, K. Jedamzik, J. March-Russell, and S. M. West, *Freeze-In Production of FIMP Dark Matter*, *JHEP* **03** (2010) 080, [[0911.1120](#)].
- [21] E. W. Kolb and M. S. Turner, *The Early Universe*, vol. 69. 1990.
- [22] A. Berlin and N. Blinov, *Thermal Dark Matter Below an MeV*, *Phys. Rev. Lett.* **120** (2018), no. 2 021801, [[1706.07046](#)].
- [23] A. Berlin and N. Blinov, *Thermal neutrino portal to sub-MeV dark matter*, *Phys. Rev. D* **99** (2019), no. 9 095030, [[1807.04282](#)].
- [24] C. Boehm, M. J. Dolan, and C. McCabe, *Increasing N_{eff} with particles in thermal equilibrium with neutrinos*, *JCAP* **12** (2012) 027, [[1207.0497](#)].
- [25] G.-y. Huang, T. Ohlsson, and S. Zhou, *Observational Constraints on Secret Neutrino Interactions from Big Bang Nucleosynthesis*, *Phys. Rev.* **D97** (2018), no. 7 075009, [[1712.04792](#)].
- [26] K. N. Abazajian and J. Heeck, *Observing Dirac neutrinos in the cosmic microwave background*, *Phys. Rev. D* **100** (2019) 075027, [[1908.03286](#)].

- [27] X. Luo, W. Rodejohann, and X.-J. Xu, *Dirac neutrinos and N_{eff} . Part II. The freeze-in case*, *JCAP* **03** (2021) 082, [[2011.13059](#)].
- [28] X. Luo, W. Rodejohann, and X.-J. Xu, *Dirac neutrinos and N_{eff}* , *JCAP* **06** (2020) 058, [[2005.01629](#)].
- [29] S.-P. Li and X.-J. Xu, *Neutrino magnetic moments meet precision N_{eff} measurements*, *JHEP* **02** (2023) 085, [[2211.04669](#)].
- [30] S.-P. Li and X.-J. Xu, *N_{eff} constraints on light mediators coupled to neutrinos: the dilution-resistant effect*, *JHEP* **10** (2023) 012, [[2307.13967](#)].
- [31] P. Gondolo and G. Gelmini, *Cosmic abundances of stable particles: Improved analysis*, *Nucl. Phys. B* **360** (1991) 145–179.
- [32] **Planck Collaboration**, N. Aghanim *et al.*, *Planck 2018 results. VI. Cosmological parameters*, *Astron. Astrophys.* **641** (2020) A6, [[1807.06209](#)]. [Erratum: *Astron. Astrophys.* 652, C4 (2021)].
- [33] P. F. de Salas and S. Pastor, *Relic neutrino decoupling with flavour oscillations revisited*, *JCAP* **07** (2016) 051, [[1606.06986](#)].
- [34] M. Escudero Abenza, *Precision early universe thermodynamics made simple: N_{eff} and neutrino decoupling in the Standard Model and beyond*, *JCAP* **05** (2020) 048, [[2001.04466](#)].
- [35] K. Akita and M. Yamaguchi, *A precision calculation of relic neutrino decoupling*, *JCAP* **08** (2020) 012, [[2005.07047](#)].
- [36] J. J. Bennett, G. Buldgen, P. F. De Salas, M. Drewes, S. Gariazzo, S. Pastor, and Y. Y. Y. Wong, *Towards a precision calculation of N_{eff} in the Standard Model II: Neutrino decoupling in the presence of flavour oscillations and finite-temperature QED*, *JCAP* **04** (2021) 073, [[2012.02726](#)].
- [37] M. Cielo, M. Escudero, G. Mangano, and O. Pisanti, *N_{eff} in the Standard Model at NLO is 3.043* , [[2306.05460](#)].
- [38] **Simons Observatory Collaboration**, M. H. Abitbol *et al.*, *The Simons Observatory: Astro2020 Decadal Project Whitepaper*, *Bull. Am. Astron. Soc.* **51** (2019) 147, [[1907.08284](#)].
- [39] **Simons Observatory Collaboration**, P. Ade *et al.*, *The Simons Observatory: Science goals and forecasts*, *JCAP* **02** (2019) 056, [[1808.07445](#)].
- [40] K. Abazajian *et al.*, *CMB-S4 Science Case, Reference Design, and Project Plan*, [[1907.04473](#)].
- [41] **CMB-S4 Collaboration**, K. N. Abazajian *et al.*, *CMB-S4 Science Book, First Edition*, [[1610.02743](#)].
- [42] **CMB-HD Collaboration**, S. Aiola *et al.*, *Snowmass2021 CMB-HD White Paper*, [[2203.05728](#)].
- [43] M. Viel, J. Lesgourgues, M. G. Haehnelt, S. Matarrese, and A. Riotto, *Constraining warm dark matter candidates including sterile neutrinos and light gravitinos with wmap and the lyman-alpha forest*, *Phys. Rev. D* **71** (2005) 063534, [[astro-ph/0501562](#)].
- [44] M. Viel, G. D. Becker, J. S. Bolton, and M. G. Haehnelt, *Warm dark matter as a solution to the small scale crisis: New constraints from high redshift lyman- α forest data*, *Phys. Rev. D* **88** (2013) 043502, [[1306.2314](#)].

- [45] J. Baur, N. Palanque-Delabrouille, C. Yèche, A. Boyarsky, O. Ruchayskiy, E. Armengaud, and J. Lesgourgues, *Constraints from Ly- α forests on non-thermal dark matter including resonantly-produced sterile neutrinos*, *JCAP* **12** (2017) 013, [[1706.03118](#)].
- [46] V. Iršič *et al.*, *New constraints on the free-streaming of warm dark matter from intermediate and small scale lyman- α forest data*, *Phys. Rev. D* **96** (2017), no. 2 023522, [[1702.01764](#)].
- [47] N. Palanque-Delabrouille, C. Yèche, N. Schöneberg, J. Lesgourgues, M. Walther, S. Chabanier, and E. Armengaud, *Hints, neutrino bounds and wdm constraints from sdss dr14 lyman- α and planck full-survey data*, *JCAP* **04** (2020) 038, [[1911.09073](#)].
- [48] A. Garzilli, A. Magalich, O. Ruchayskiy, and A. Boyarsky, *How to constrain warm dark matter with the lyman- α forest*, *Mon. Not. Roy. Astron. Soc.* **502** (2021), no. 2 2356–2363, [[1912.09397](#)].
- [49] J. Heeck and D. Teresi, *Cold keV dark matter from decays and scatterings*, *Phys. Rev. D* **96** (2017), no. 3 035018, [[1706.09909](#)].
- [50] Q. Decant, J. Heisig, D. C. Hooper, and L. Lopez-Honorez, *Lyman- α constraints on freeze-in and superWIMPs*, *JCAP* **03** (2022) 041, [[2111.09321](#)].
- [51] R. Coy, T. Hambye, M. H. G. Tytgat, and L. Vanderheyden, *Domain of thermal dark matter candidates*, *Phys. Rev. D* **104** (2021), no. 5 055021, [[2105.01263](#)].
- [52] **Particle Data Group Collaboration**, R. L. Workman *et al.*, *Review of Particle Physics*, *PTEP* **2022** (2022) 083C01.
- [53] E. Vitagliano, I. Tamborra, and G. Raffelt, *Grand Unified Neutrino Spectrum at Earth: Sources and Spectral Components*, *Rev. Mod. Phys.* **92** (2020) 45006, [[1910.11878](#)].
- [54] **PTOLEMY Collaboration**, E. Baracchini *et al.*, *PTOLEMY: A Proposal for Thermal Relic Detection of Massive Neutrinos and Directional Detection of MeV Dark Matter*, [[1808.01892](#)].
- [55] **PTOLEMY Collaboration**, M. G. Betti *et al.*, *Neutrino physics with the PTOLEMY project: active neutrino properties and the light sterile case*, *JCAP* **07** (2019) 047, [[1902.05508](#)].
- [56] Y. Cheipesh, V. Cheianov, and A. Boyarsky, *Navigating the pitfalls of relic neutrino detection*, *Phys. Rev. D* **104** (2021), no. 11 116004, [[2101.10069](#)].
- [57] **PTOLEMY Collaboration**, A. Apponi *et al.*, *Heisenberg’s uncertainty principle in the PTOLEMY project: A theory update*, *Phys. Rev. D* **106** (2022), no. 5 053002, [[2203.11228](#)].
- [58] R. Mertig, M. Bohm, and A. Denner, *FEYN CALC: Computer algebraic calculation of Feynman amplitudes*, *Comput. Phys. Commun.* **64** (1991) 345–359.
- [59] V. Shtabovenko, R. Mertig, and F. Orellana, *New Developments in FeynCalc 9.0*, *Comput. Phys. Commun.* **207** (2016) 432–444, [[1601.01167](#)].
- [60] V. Shtabovenko, R. Mertig, and F. Orellana, *FeynCalc 9.3: New features and improvements*, *Comput. Phys. Commun.* **256** (2020) 107478, [[2001.04407](#)].
- [61] H. H. Patel, *Package-X: A Mathematica package for the analytic calculation of one-loop integrals*, *Comput. Phys. Commun.* **197** (2015) 276–290, [[1503.01469](#)].
- [62] H. H. Patel, *Package-X 2.0: A Mathematica package for the analytic calculation of one-loop integrals*, *Comput. Phys. Commun.* **218** (2017) 66–70, [[1612.00009](#)].